Structural origin of long-range proximity effect in highly disordered fractal MgO/MgB_2 nanocomposites: Roles of interface, geometry and defect

Iku Nakaaki,[1] Aoi Hashimoto,[1] Shun Kondo,[2] Yuichi Ikuhara,[2,3] Shuuichi Ooi,[4] Minoru Tachiki, [4] Shunichi Arisawa,[5] Akiko Nakamura,[6] Taku Moronaga,[6] Jun Chen,[7] Hiroyo Segawa,[7] Takahiro Sakurai,[8] Hitoshi Ohta,[9] and Takashi Uchino[1,a)*]

[1] *Department of Chemistry, Graduate School of Science, Kobe University, Kobe 657-8501, Japan*
[2] *Institute of Engineering Innovation, School of Engineering, The University of Tokyo, Tokyo 113-8656, Japan*
[3] *Advanced Institute for Materials Research (AIMR), Tohoku University, Sendai 980-8577, Japan*
[4] *International Center for Materials Nanoarchitectonics (MANA), National Institute for Materials Science, Tsukuba 305-0047, Japan*
[5] *Research Center for Functional Materials, National Institute for Materials Science, Tsukuba 305-0047, Japan*
[6] *Research Network and Facility Services Division, National Institute for Materials Science, Tsukuba 305-0047, Japan*
[7] *Research Center for Electronic and Optical Materials, National Institute for Materials Science, Tsukuba 305-0044, Japan*
[8] *Center for Support to Research and Education Activities, Kobe University, Kobe 657-8501, Japan*
[9] *Molecular Photoscience Research Center, Kobe University, Kobe 657-8501, Japan*

ABSTRACT. The emergence of global phase coherence due to proximity effect in heterogeneous and disordered superconductor systems has been an issue of long-standing interest. Recently, we have reported that a highly disordered fractal MgO/MgB_2 nanocomposite exhibits bulk-like superconducting properties with isotropic pinning, showing an excellent phase-coherent capability irrespective of the low volume fraction (~30 vol. %) of MgB_2 [Uchino *et al*., Phys. Rev. B **101**, 035146 (2020); Teramachi *et al*,, Phys. Rev. B **108**, 155146 (2023)]. In this work, we show from 3D focused ion beam scanning electron microscopy data that in the nanocomposite, a complex MgO/MgB_2 microstructure spreads isotropically throughout the sample with a constant fractal dimension of ~1.67. Atomic-resolution scanning transmission electron microscopy has revealed that the interfaces are atomically clean and free from amorphous grain boundaries. Detailed ac susceptibility measurements have demonstrated a smooth crossover from an intragranular to an intergranular superconducting regime. Also, spatially-resolved cathodoluminescence measurements have demonstrated that oxygen vacancies in the MgO-rich phase tend to aggregate near the MgO/MgB_2 boundary regions, forming long channels of oxygen vacancies through the nanocomposite. These channels of oxygen vacancies are likely to be responsible for the long-range carrier transfer and the related proximity effect via coherent tunneling of charge carriers among the oxygen vacancy sites. Our results imply that the fractal-like MgO/MgB_2 microstructure with atomically clean interfaces will induce the phase coherent transport of charge carries in the MgO-rich regions, leading to the observed long-range proximity effect and the resulting bulk-like superconductivity in this highly disordered system.

[a)] Author to whom correspondence should be addressed: uchino@kobe-u.ac.jp

I. INTRODUCTION.

The quality and geometry of the interface between a normal metal（N） and a superconductor (S) plays a critical role in the transmission of a supercurrent through any SNS structure [1−5]. In the SNS junctions with highly transparent interfaces, a supercurrent can flow through nominally non-superconducting materials even over a length scale ranging from hundreds of nanometers to micrometers [6–8]. Accordingly, the normal metal may acquire genuine superconducting properties, resulting in proximity-induced superconductivity in a macroscopic length scale. Microscopically, this effect, known as proximity effect, is mediated by Andreev reflections, where incident electrons are converted into holes in the normal metal creating Cooper pairs in the superconductor [9,10]. Thus far, lots of efforts have been made to fabricate clean and transparent SNS interfaces to investigate the nature of the proximity effect by using, for example, layer-by-layer grown thin films [11,12], and carefully designed van der Waals 2D materials [13]. Furthermore, artificial superlattices with clean interfaces have also been fabricated to investigate the effect of nanoscale geometry on superconductivity in the quantum wells [14,15]. Then, it has been demonstrated that the proximity effects and the related superconducting states are influenced not only by the quality of interface but also by its short- and long-range geometry, e.g., the curvature of the junction [11], the nanoscale building blocks [14,15], and the degree of disorder [16]. This implies that the proximity effect is greatly affected by the geometric conditions of the system of interest over the wide length scale.

In comparison to the case of thin films, quantum wells and artificial 2D systems, however, the geometric effect on the proximity effect in 3D nanocomposites has hardly been investigated. Although the proximity effect of granular 3D superconductors has been extensively studied, the experimental research interest has been mainly focused on the effect of size and ratio of S/N grains on the superconducting properties of the composite [17−19]. This is mainly due to the fact that in granular systems, it is difficult to control the shape and the geometry of the S/N grains and their interface characteristics. In the interface regions, there exist, in general, dislocations, impurities, voids and amorphous phases, all of which potentially suppress Andreev reflections and hence the proximity effect.

Zhang *et al*. [20] have previously reported that when MgO/MgB_2 composites are prepared by using the solid phase reaction between Mg and B_2O_3, i.e., $4Mg+B_2O_3 \rightarrow 3MgO + MgB_2$, the resistance ($R$) vs temperature ($T$) curve of the resulting $3MgO\text{-}MgB_2$ composite shows a superconducting transition (onset) at 38.0 K, finally leading to a zero resistance state at 36.0 K. Since the mole fraction of MgO is rather high (~75 %), the resulting zero resistance may not be due to the proximity effect but can be interpreted in terms of a statistical percolation model [20]. Recently, we [21,22] have reported that when this $3MgO\text{-}MgB_2$ composite powder is sintered by a spark plasma sintering (SPS) technique, the sintered material acts as a bulk-like superconductor, showing not only zero resistivity but also perfect diamagnetism and isotropic pinning. The observation of perfect diamagnetism implies that a fully phase-coherent state is established over the entire region of the sample, including the MgO-rich regions, via the proximity effect. SPS is an unconventional sintering technique, which combines simultaneous heating by dc current pulses with application of uniaxial pressure, and hence provides an exceptional advantage of fast heating/cooling rates when compared with conventional sintering methods [23]. The short exposition of materials to high temperature during SPS will not result in the undesired grain growth but may help to create well-ordered clean interfaces favorable for the proximity effect. We [21,22] have also demonstrated from electron microscopy imaging techniques that the SPS-treated MgO/MgB_2 nanocomposites are characterized by scale-free (or fractal) distribution of MgB_2 components. It is hence most likely that the unique geometrical features induced by the SPS process play a vital role in establishing the long-range proximity effect and the resultant bulk-like superconductivity.

To get deeper insights into the geometrical influences on the superconducting properties of the thus prepared MgO/MgB_2 fractal nanocomposite, we here perform detailed structural analyses using focused ion beam scanning electron microscopy (FIB-SEM) and scanning transmission electron microscope (STEM) imaging. The 2D observation of FIB-SEM cross-sectional images allows us to reconstruct 3D images of the original sample, which can enable characterization of fractality of the sample over its entire volume via the resulting 3D images. High-angle annular dark field STEM (HAADF-STEM) and annular bright-field STEM (ABF-STEM) images have unambiguously demonstrated that the MgO/MgB_2 boundaries are characterized by atomically clean and sharp interfaces with a terrace-and-step morphology. Furthermore, we carried out a series of ac susceptibility measurements as well as detailed MO imaging analysis to investigate the applicability of the critical state model to this proximity-induced system. Finally, on the basis of the results of chathode-luminescence (CL) measurements, we discuss a possible role of oxygen vacancies in the MgO-rich region in terms of the phase coherent transport of

charge carries in the MgO-rich regions responsible for the long-range proximity effect.

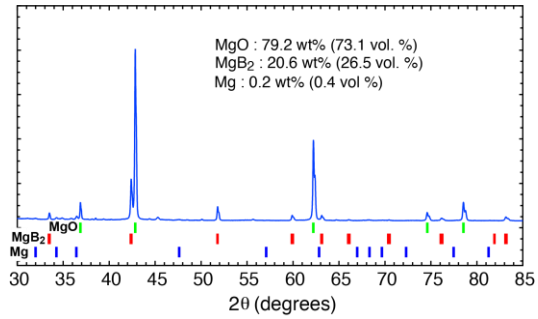

FIG.1. XRD pattern and output from quantitative Rietveld analysis of the bulk sintered sample prepared with SPS at a temperature of ~1200 ºC.

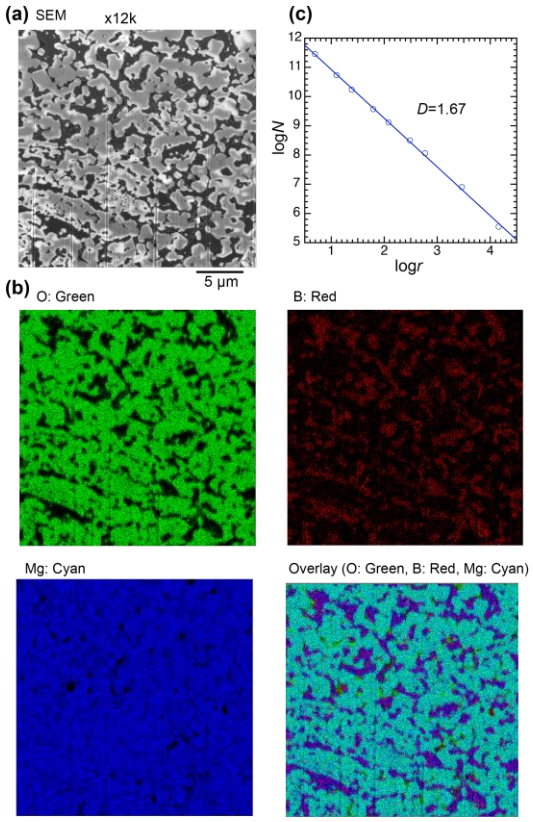

FIG. 2. (a) SEM and (b) the corresponding EDX images of the Ga-ion etched surface; Green = O, Red = B, and Blue = Mg. (c) The box-counting analysis for boron distribution in the SEM/EDX image given in (b).

II. EXPERIMENTAL PROCEDURES

The MgO/MgB_2 fractal nanocomposites were prepared by the solid-phase reaction of Mg and B_2O_3 powders under Ar atmosphere at 700 °C, followed by a subsequent SPS procedure with a uniaxial pressure of 114 MP at ~1200 °C under vacuum, as reported in our previous papers [21,22]. The resulting bulk samples were cut into appropriate shapes depending on the measurement techniques, including x-ray diffraction (XRD), SEM/energy-dispersive x-ray spectroscopy (SEM-EDX), FIB-SEM, STEM, magnetoresistivity, ac and dc magnetization, MO imaging, and CL spectroscopy. Details of the sample preparation and characterization procedures are given in the supplementary material.

III. RESULTS

A. Structural and morphological properties

Figure 1 shows a typical XRD pattern of the solid sintered sample after SPS at ~1200 °C. From the XRD pattern and the Rietveld pattern fitting, we found that the sample consists of MgO (79.2 wt %), MgB_2 (20.6 wt %) and a small amount of Mg (0.2 wt %), corresponding to the approximate volume fraction of MgO 73.1 %, MgB_2 26.5 %, and Mg 0.4 %. The morphology and elemental distribution of the Ga-ion etched surface was investigated by SEM-EDX analysis, as shown in Fig. 2. From the SEM image given in Fig. 2(a), one sees gray and black regions,

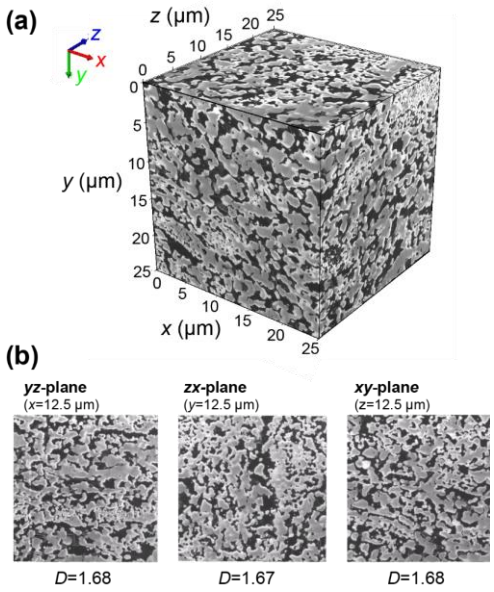

FIG. 3. (a) 3D image reconstructed from the FIB/SEM serial sectioning images (Multimedia available online). (b) Cross-sectional images sliced at *x*=12.5, y=12.5 and z=12.5 μm along the *yz*, the *zx* and the *xy* planes, respectively, obtained from the 3D reconstructed image. The box-counting fractal dimension *D* is given for each image.

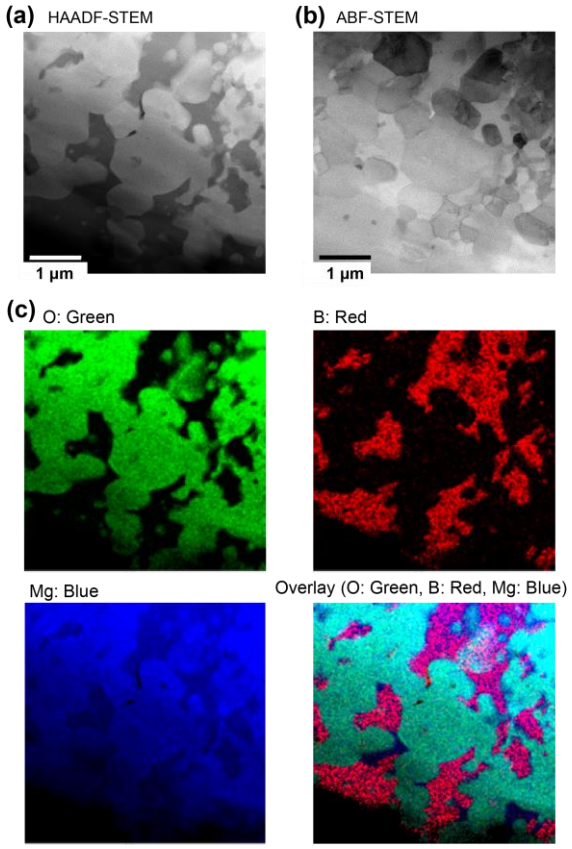

FIG. 4. (a) HAADF-STEM and (b) ABF-STEM images and (c) the corresponding STEM/EDX images; Green = O, Red = B, and Blue = Mg.

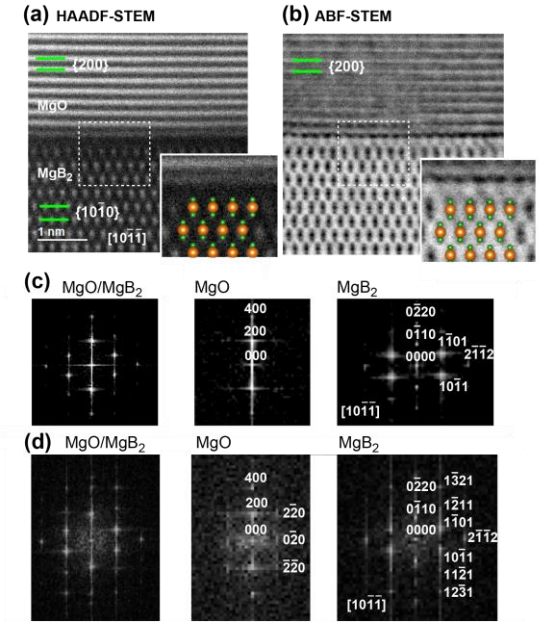

FIG. 5. (a) HAADF-STEM and (b) ABF-STEM images of a planar MgO/MgB_2 interface. The insets in (a) and (b) indicate the enlarged images of the white box regions, along with possible atomic arrangements of Mg (orange) and B (green) atoms. (c), (d) FFT images of (a) and (b), respectively. In (c) and (d), the left panel shows the FFT image of the whole STEM image, whereas the middle and right panels are the FFT images of the MgO- and MgB_2-rich regions, respectively, of the corresponding STEM images.

which are characterized by a complicated interwove-like structure. The SEM-EDX mapping images revealed that the oxygen (green) and boron (red) distributions almost match with the gray and black regions in the corresponding SEM image. Hence, it is reasonable to assume that the gray and black region in the SEM image correspond to the MgO- and MgB_2-rich regions, respectively. The box-counting fractal dimension D obtained from the binary-converted SEM image is 1.67 [Fig. 2(c)], confirming the fractal nature of the MgO/MgB_2 distribution. We then conducted the 3D reconstruction of the MgO/MgB_2 distribution from the sequential FIB-SEM images, as shown in Fig. 3(a) (Multimedia available online). The resulting cross sectional images are illustrated in Fig. 3(b). We found that the disordered microstructures are isotropically distributed, yielding almost constant values of D (D = 1.67–1.68) irrespective of the direction of the cross section employed. This indicates that the fractal and interwoven-like MgO/MgB_2 structures spread isotropically throughout the sample. In this work, the bulk sintered sample was prepared by the SPS process with a uniaxial pressure of 114 MPa. From the observed isotropic morphology, we can say that the uniaxial compression during the SPS process hardly affects the spatial distribution and local morphology of the MgO and MgB_2 grains.

We next investigate the structural characteristics of the nanocomposite in the micro- and nanometer ranges using STEM. Figure 4 shows HAADF-STEM and ABF-STEM images along with the STEM-EDX elemental mapping. As in the case of SEM and SEM-EDX images shown in Fig. 2, the complex or fractal-like structures can be recognized in these STEM and STEM-EDX images of higher magnifications. It should also be noted that the MgB_2-rich regions, which are represented by red irregular shapes in the STEM-EDX image shown in Fig. 4(c), are not physically attached to each other but are separated by the surrounding MgO-rich regions. Thus, in the submicrometer range, the present nanocomposite can be regarded as 3D ensembles of randomly interconnected MgB_2/MgO/MgB_2 junctions.

Figures 5 and 6 show HAADF-STEM and ABF-STEM images of planar (straight) MgO/MgB_2

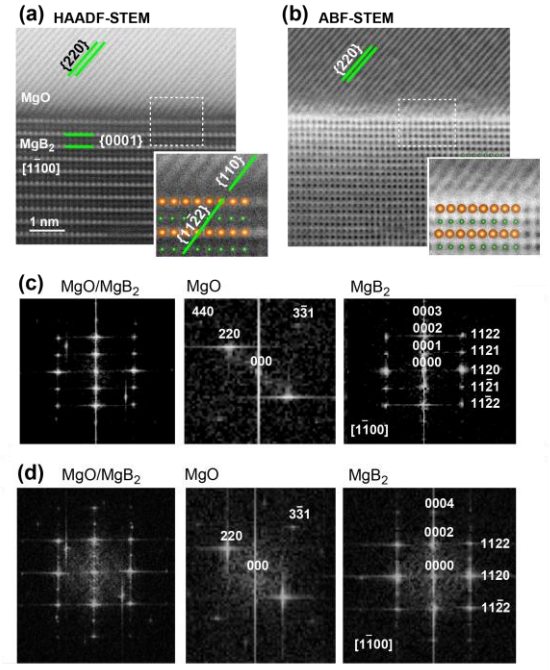

FIG. 6. (a) HAADF-STEM and (b) ABF-STEM images of another planar MgO/MgB_2 interface. The insets in (a) and (b) indicate the enlarged images of the white box regions, along with possible atomic arrangements of Mg (orange) and B (green) atoms. (c), (d) FFT images of (a) and (b), respectively. In (c) and (d), the left panel shows the FFT image of the whole STEM image, whereas the middle and right panels are the FFT images of the MgO- and MgB_2-rich regions, respectively, of the corresponding STEM images.

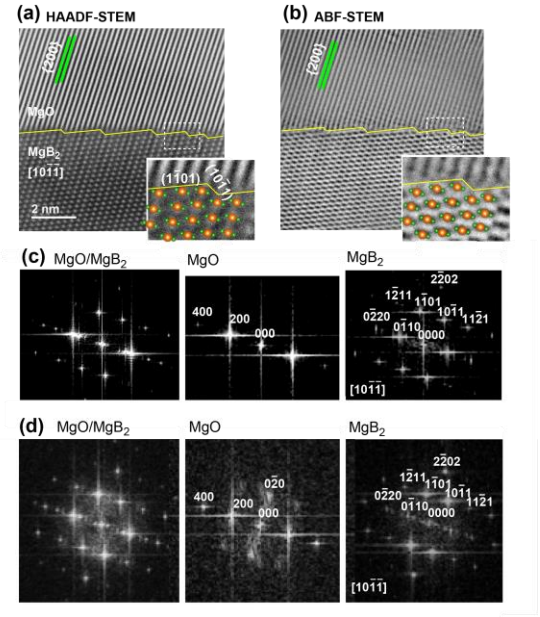

FIG. 7. (a) HAADF-STEM and (b) ABF-STEM images of a terraced MgO/MgB_2 interface. Nanometer length-scale steps are visible (marked as a solid yellow line). The insets in (a) and (b) indicate the enlarged images of the white box regions, along with possible atomic arrangements of Mg (orange) and B (green) atoms. (c), (d) FFT images of (a) and (b), respectively. In (c) and (d), the left panel shows the FFT image of the whole STEM image, whereas the middle and right panels are the FFT images of the MgO- and MgB_2-rich regions, respectively, of the corresponding STEM images.

boundaries. In Fig. 5, the $\{10\bar{1}0\}$-type planes of MgB_2 and the {100}-type planes of MgO are aligned in the same direction, as also demonstrated in the corresponding fast Fourier transform (FFT) images. The MgO/MgB_2 interface is atomically clean and flat without forming an interfacial amorphous phase, although the amorphous region is very often observed in the grain boundaries of polycrystalline materials [24,25]. We also found another type of clean and planar interface (Fig. 6), where the crystallographic directions of the MgO and MgB_2 phases appear to be different to each other. We note, however, that a close look at the FFT images reveal the alignment of the {110}-type planes of MgO and the $\{11\bar{2}2\}$-type planes of MgB_2 (see also the inset of Fig. 6(a)), forming a pseudo-semicoherent interface [25].

It should further be mentioned that in the nanocomposite, there exist several non-planar interfaces, as shown in Figs. 7 and 8. In the STEM images given in Fig. 7, the MgB_2 phase is oriented in the $[10\bar{1}\bar{1}]$ zone axis and the MgO/MgB_2 interface is not straight. Even in such a case, one sees that an atomically clean boundary is established by forming a terrace-and-step structure at the MgO/MgB_2 interface. The steps were identified to be parallel to the $\{10\bar{1}1\}$-type planes such as $(10\bar{1}1)$ and $(1\bar{1}01)$ planes of MgB_2 [see the insets of Fig. 7(a),(b)]. Similar atomically clean MgO/MgB_2 interfaces with a terrace-and-step morphology can also be found in the triple junction consisting of one MgB_2 and two differently aligned MgO phases (Fig. 8). In this triple junction, all the constituent boundaries, including the MgO/MgO boundary, are free of amorphous phase as well. A terrace-and-step structure, which is along low-index planes of MgB_2, including $(1\bar{1}01)$ and $(0\bar{1}10)$ planes (see also the inset of Fig. 8(a),(b)), can be recognized at the interface between the MgB_2 and MgO(2) phases. The general formation of these terrace-and-step structures at the MgO/MgB_2 interface regions implies the motion and/or dynamic adjustment of grain boundaries [26–30] during the SPS process. We hence suggest that in the grain boundaries, dynamic structural transformation accommodates the SPS-induced microstructural evolution, resulting in

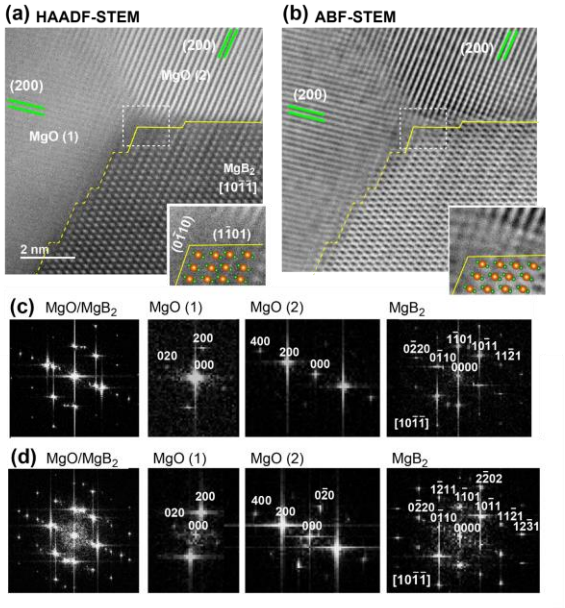

FIG. 8. (a) HAADF-STEM and (b) ABF-STEM images of a triple junction consisting of one MgB_2 and two differently aligned MgO phases, namely MgO(1) and MgO(2). Nanometer length-scale steps are visible especially between MgB_2 and MgO(2) (marked as a solid yellow line). As for the boundary between MgB_2 and MgO(1), the specimen is slightly tilted from the edge-on condition, yielding a somewhat blurred interface (marked as a broken yellow line). The insets in (a) and (b) indicate the enlarged images of the white box regions, along with possible atomic arrangements of Mg (orange) and B (green) atoms. (c), (d) FFT images of (a) and (b), respectively. In (c) and (d), the left panel shows the FFT image of the whole STEM image, whereas the two middle and right panels are the FFT images of the MgO(1), MgO(2) and MgB_2-rich regions, respectively, of the corresponding STEM images.

atomically clean interfaces without creating any voids, cracks and interfacial amorphous regions.

The above FIB-SEM and STEM investigations on the MgO/MgB_2 nanocomposite not only demonstrated the isotropic fractal structure, but they also revealed the formation of atomically clean interfaces between MgO and MgB_2 phases. It is most likely that these unique structural and morphological characteristics are reflected in the Andreev reflection process and the related superconducting proximity effect, as has already been inferred in our previous studies [21,22].

B. Basic superconducting properties

Figure 9(a) shows the temperature dependence of ρ measured in the temperature range from 2 to 300 K. One sees the onset of superconductivity at 38.4 K, followed by the zero-resistance state at temperatures below 36.6 K. A similar superconducting transition

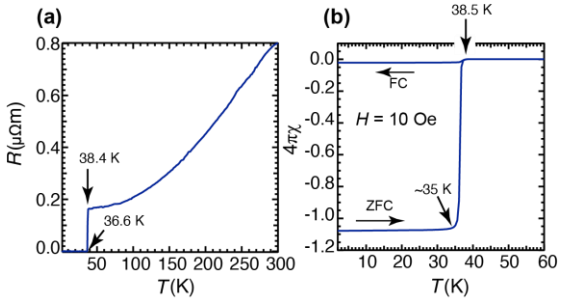

FIG. 9. (a) Temperature-dependent resistivity. (b) Zero-field-cooling (ZFC) and field-cooling (FC) magnetic susceptibility (4πχ) curves under dc applied field of 10 Oe.

can also be recognized in the zero-filed-cooling (ZFC) and field-cooling (FC) dc magnetic susceptibility (4πχ) curves [Fig. 9(b)]. The ZFC susceptibility curve is decreased sharply below the onset temperature at 38.5 K and shows an almost constant value of −1.1 at temperatures below ~35 K. We should note that in this work, the dc magnetization measurements were carried out for a square cuboid-shape sample with a dimension of $1\times1\times5$ mm^3 by applying a magnetic field H along the long side of the sample. In this experimental set up, the effective demagnetization factor D is estimated to be ~0.05 [31]. Thus, a slight discrepancy from the ideal perfect diamagnetism ($4\pi\chi=-1$) is due to a possible demagnetization effect. On the other hand, the FC curve shows a very low Meissner fraction (<~1%), illustrating the strong pinning nature of the present MgO/MgB_2 nanocomposite. The temperature-dependence of ρ and M shown above are in good agreement with those reported previously for the similarly prepared MgO/MgB_2 sample [22], demonstrating an excellent reproducibility of the superconducting properties of these fractal nanocomposites.

The temperature dependence of the lower critical fields $H_{c1}(T)$ was evaluated from the initial $M(H)$ ZFC curves shown in Fig. S1 in the supplementary material. From the extrapolated value at zero temperature, $H_{c1}(0)$ is estimated to be 713 Oe (see Fig. S1(c) in the supplementary material). The upper critical field H_{c2} was obtained from the magnetoresistivity measurements (see Fig. S2 in the supplementary material). In this work, $H_{c2}(T)$ was defined as the applied field for which the sample resistance measured at T is 10 % of the normal state value. The $H_{c2}(T)$ curve was fitted with $H_{c2}(T) = H_{c2}(0)(1-T/T_c)^{1+\alpha}$, where the parameter $\alpha>0$ describes the positive curvature of $H_{c2}(T)$ (see Fig. S2(b) in the supplementary material). The fitted values of α and $H_{c2}(0)$ are found to be 0.23 and 97.9 kOe, respectively.

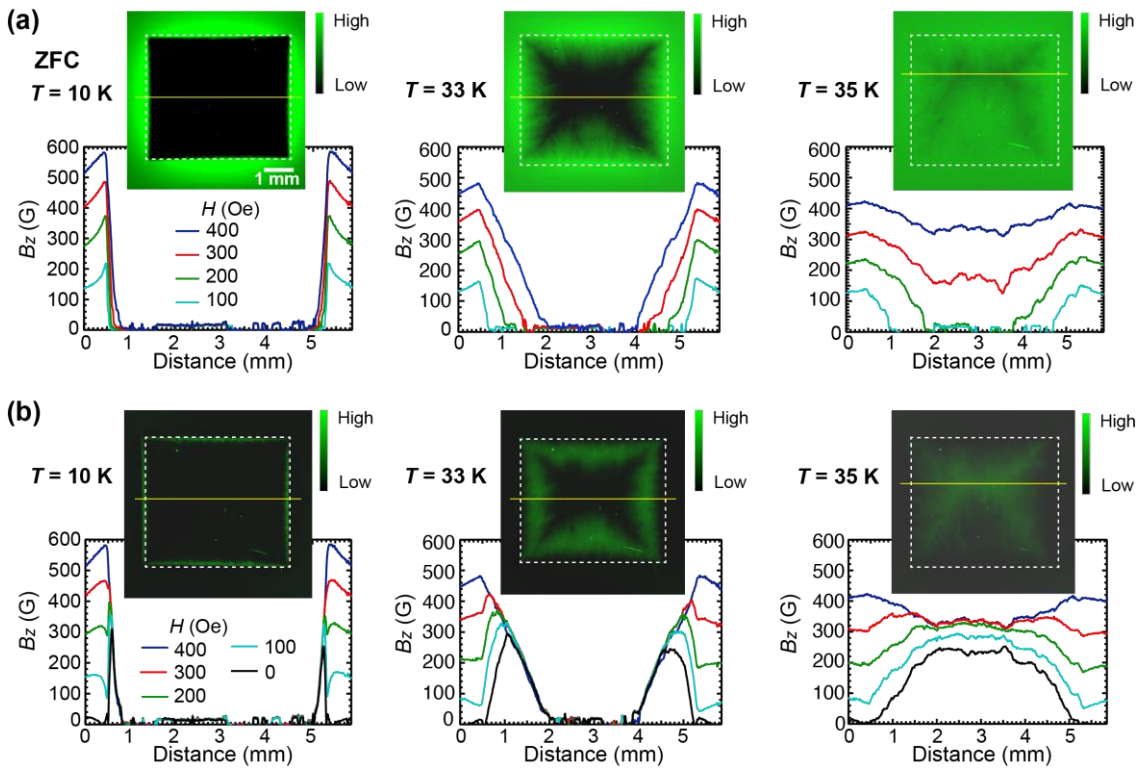

FIG. 10. MO observations after ZFC to different temperatures. (a) Profiles of perpendicular magnetic flux density B_z along the yellow line of the inset during the ramp-up stage of H from 100 to 400 Oe. The respective insets show the MO images obtained in an applied field of 400 Oe. (b) Profiles of B_z along the yellow line of the inset during the ramp-down stage of H from 400 to 0 Oe. The respective insets show the MO images in the remanent (H = 0 Oe) state showing trapped magnetic flux. The white dashed line in the insets indicates the edge of the sample.

From the values of $H_{c1}(0)$ = 713 Oe and $H_{c2}(0)$ = 97.9 kOe, the penetration depth λ and the coherence length ξ can be estimated to be 77.7 and 5.7 nm, respectively, on the basis of the Ginzburg-Landau (GL) theory (for the details of calculations, see the supplementary material). The obtained values of λ and ξ are also in reasonable agreement with those of our previous sample [22].

C. MO imaging measurements

In our previous paper [22], MO imaging was used to visualize magnetic flux in the MgO/MgB_2 nanocomposite; however, our previous sample used for MO imaging has a physical crack created accidentally during surface polishing. In this work, we carefully prepared a crack-free plane-parallel-plate sample with a dimension of 4.1×4.8×0.5 mm^3 for the purpose of detailed MO analysis.

In the MO imaging, the sample was first zero-field cooled to a measurement temperature from a temperature (T = ~60 K) well above the superconducting transition temperature, and a series of MO images was acquired as the magnetic field was applied perpendicular to the sample surface up to 400 Oe (Fig. 10 (a) and the left panels in Fig. S3 in the supplementary material). One sees from Fig. 10 (a) that at a temperature of 10 K, magnetic flux hardly penetrates into the sample on applying H up to 400 Oe except just along the edge, in agreement with high H_{c1} values at such a low temperature range ($H_{c1}(T) > \sim 500$ Oe for $T < \sim 10$ K, see Fig. S1 in the supplementary material). As the temperature is increased, one can recognize a partial flux penetration by applying magnetic fields up to 400 Oe (Fig. 10 (a) and the left panels in Fig. S3 in the supplementary material). Note also that at temperatures up to ~33 K, the sand-pile like behavior of the perpendicular magnetic flux density B_z can be seen during the ramp-up stage of H; i.e., the flux gradient is almost constant irrespective of H, in agreement with the Bean critical state model [32]. At temperatures near ~35 K, however, the profile of B_z becomes flat with increasing H. This indicates that in these temperature and field regions, the magnetic flux gradient along the in-plane (x-axis) direction should decrease with H and that the corresponding current density J_c should diminish, as predicted by a modified

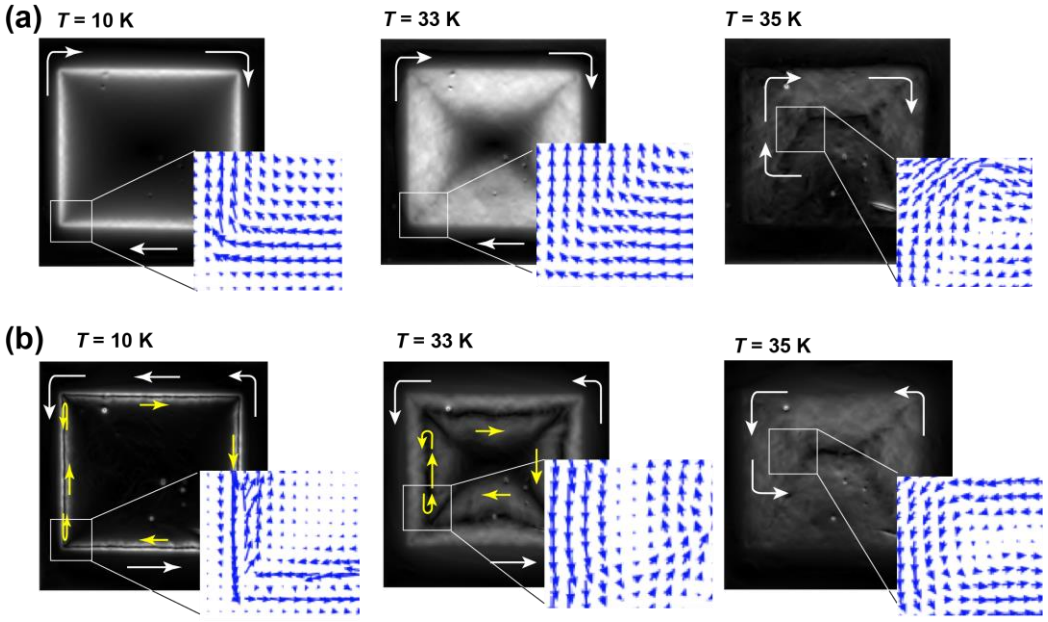

FIG. 11. (a), (b) Supercurrent density calculated from the MO images shown in the insets of Figs. 10(a), and 10(b), respectively. The white and yellow arrows qualitatively indicate the direction of the local current. The respective insets represent the calculated current of the white box region in the form of current vectors.

critical state model assuming that the critical current density is not constant, but is determined by the pinning force [33,34].

We next investigate the flux density profile during the ramp-down stage of H. As shown in Fig. 10 (b) and the right panels Fig. S3 in the supplementary material, the observed B_z profiles obtained at temperatures up to ~33 K follow the critical state model, in agreement with the results obtained in the ramp-up stage of H. Note also that at temperatures around ~35 K, where the vortices occupied the whole crystal for $H \geq \sim 300$ Oe, the vortices around the sample edges leave the sample with decreasing H, and accordingly, in the remanent state, the penetrated vortices in the near central region of the sample are strongly pinned to show a "rooftop" pattern [see the right panel in Fig. 10(b)]. In the remanent state at a temperature of 35 K, however, the ridge of the rooftop is not located in the exact middle of the sample, implying that the pinning force density is not constant over the entire volume of the sample at such a temperature close to T_c.

We should note that B_z obtained from the MO observations of a thick-plate sample is generated mainly by the sum of a two-dimensional vortex current flow in the near-surface region [35]. From this follows that a numerical inversion of Biot-Savart law can yield information on the semiquantitative current distribution in the sample surface [36] (for details, see the supplementary material). Figure 11 shows mapping of the current density and the current vectors calculated by using the corresponding MO images shown in Fig. 10. When a magnetic field is applied after ZFC, the current flows in a clockwise direction throughout the sample, implying the presence of uniform bulk current in the corresponding critical state. As for the remanent states, one sees complex current distributions flowing in a clockwise and/or an anti-clockwise direction depending on the measurement temperature. The resulting complex current flow in the remanent state is due to the redistribution of the pinned vortices during the field ramp down process and the subsequent local change in the sign of the gradient $\frac{\partial B_z}{\partial x}$, as shown in Fig. 10 (b). Thus, the current distributions provide complementary and useful information on the temperature- and field-dependent flux pinning of the present sample.

Furthermore, we measured the MO image of trapped magnetic flux in the field-cooled (FC) remanent state, which is produced by cooling the sample from ~60 to 5 K under an external magnetic field of 200 Oe and then reducing the applied field to zero. Figures 12(a) shows the MO image for the remanent state taken at 5 K, and its qualitative 3D representation is given in Fig. 12(c). We see that the magnetic flux is distributed uniformly throughout the sample, as evidenced by an almost flat profile of B_z~200 G (see the inset of Fig. 12(a)). This indicates that the vortices are strongly and uniformly pinned over the whole area of the sample,

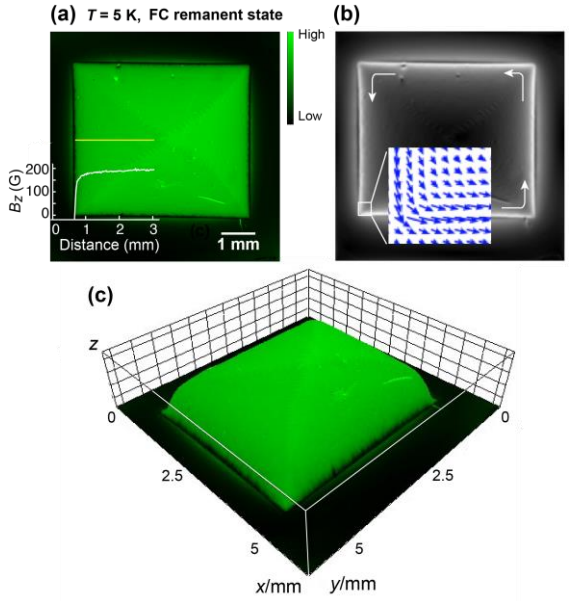

FIG. 12. (a) MO image after FC to 5 K in an applied field of 200 Oe and the reducing the applied field to zero. (b) The corresponding calculated current density. The inset in (a) represents the profile of perpendicular magnetic flux density B_z along the yellow line. The inset in (b) shows the calculated current of the white box region in the form of current vectors. The white arrows in (b) qualitatively indicate the direction of the local current. (c) Qualitative 3D representation of the MO image shown in (a).

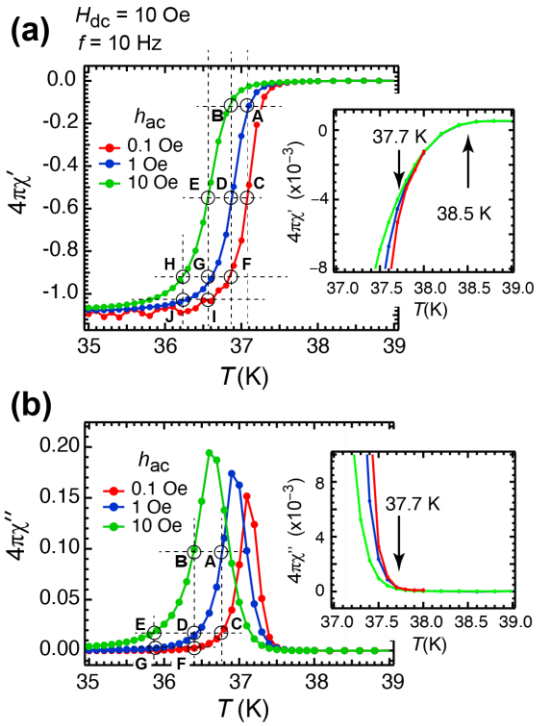

FIG. 13. Temperature dependence of the magnetic ac susceptibility [(a) $4\pi\chi'$ and (b) $4\pi\chi''$] observed in a dc magnetic field of 10 Oe using an ac frequency f of 10 Hz at three different ac amplitudes h_{ac}. The respective insets show the expanded plots near the superconducting onset temperature (T = 38.5 K).

including the MgO rich regions, at such a low temperature. Figures 12 (a) and 12(c) also revealed that the flux distribution near the edge is steeply reduced, showing a flux annihilation zone just outside the edge. Figure 12(b) gives the corresponding current distribution. One sees that a large supercurrent circulates especially around the sample edge in an anti-clockwise direction. These edge features most likely results from the uniform return field of the trapped flux [37,38]. The flux of the opposite sign penetrates an outer rim of the sample, leading to a steep drop in B_z and the corresponding edge supercurrent, together with the flux annihilation zone outside the edge.

D. AC susceptibility measurements

From a series of MO images demonstrated in the above subsection, one can notice that the present MgO/MgB_2 nanocomposite does not show any granular behaviors in terms of flux entry, exit and pinning, but it exhibits good electromagnetic homogeneity at least at temperatures below ~36 K. To get an additional insight into the superconducting properties in the temperature region above ~36 K, we employed the ac magnetic susceptibility method, which is a useful technique for the analysis of the electromagnetic properties of various forms of superconductors (single crystals, polycrystals, films, etc), especially under weak magnetic fields just below T_c.

Figure 13 shows the temperature-dependent ac susceptibility of the MgO/MgB_2 nanocomposite with a dimension of 1×1×5 mm^3 measured in a static (dc) magnetic field of H = 10 Oe with different ac excitation amplitudes h_{ac} and a constant frequency f of 10 Hz. The magnetic field is applied along the long side of the sample, as in the case of the dc susceptibility measurements. The real ($4\pi\chi'$) susceptibility given in Fig. 13(a) shows an onset of superconductivity at 38.5 K and reaches ~−1 at T~35 K, in agreement with those obtained from the dc magnetization measurements [see Fig. 9(b)]. In the temperature range from 37.7 to 38.5 K, the $4\pi\chi'$ curves are almost independent of h_{AC}, and the imaginary ($4\pi\chi''$) susceptibility remains to be zero. This h_{AC}-independent feature of the ac susceptibility can be interpreted in terms of the intragranular superconductivity [39,40]. At temperatures below

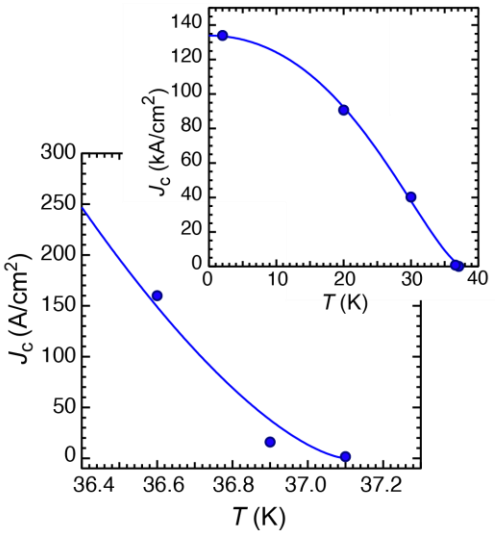

FIG. 14. Critical current density J_c as a function of temperature T derived from the ac susceptibility data of Fig. 13(a). Solid line represents fit of function $J_c \propto (1 - T/T_c)^{3/2}$. The inset includes the lower-temperature ($T \leq$ 30K) J_c values derived from the height of the magnetization loop at zero magnetic field on the basis of the Bean model (for details, see the supplementary material). The solid line in the inset represents the temperature dependence of the depairing critical current density according to Eq. (1).

37.7 K, both the real and imaginary parts of the ac susceptibility show a strong dependence of h_{AC}. The large decrease of $4\pi\chi'$ as well as the dissipative peak in $4\pi\chi''$ results from the intergranular superconducting properties [39,40]. The observed strong h_{AC}-dependence of the ac susceptibility in the regime of intergranular superconductivity is a consequence of the nonlinearity in the electromagnetic response and can be described within the framework of the critical state model [32].

To further prove that the critical state model is applicable to the present ac susceptibility data, we employed a geometrical test proposed by Civale *et al.* [41]. In the critical state for a given sample, $4\pi\chi'$ and $4\pi\chi''$ is a only a function of ac penetration length $D_c = \frac{c}{4\pi}\left(\frac{h_{ac}}{J_c}\right)$, where c is the velocity of light, and beyond D_c the ac field is totally screened. Consequently, every horizontal line for the $4\pi\chi'$ and $4\pi\chi''$ curves shown in Fig. 13 corresponds to a constant value of D_c. On the other hand, every vertical line corresponds to a constant value of J_c as J_c is only a function of temperature. This implies that J_c(A)=J_c(C), where A (h_{ac}= 1 Oe) and C (h_{ac}= 0.1 Oe) are points located in the same vertical line in Figs. 13(a) and 13(b). The point B, with the same D_c as point A, belongs to the curve h_{ac} = 10 Oe. Since the critical state model establishes that $J_c \propto h_{ac}/D_c$, we get J_c(B)=10J_c(A). Similarly, the point D of the curve of h_{ac}= 1 Oe has the same D_c as the point C, which is the curve of h_{ac}= 0.1 Oe, and hence J_c(D)=10J_c(C). The consequence is that J_c(B)=J_c(D), implying that the points B and D should be located in the same vertical line (or the same T), as indeed graphically confirmed in both the $4\pi\chi'$ and $4\pi\chi''$ curves shown in Figs. 13(a) and 13(b). The occurrence of other rectangles, such as DEFG and/or GHIJ in the $4\pi\chi''$ and/or $4\pi\chi'$ curves, further confirms the validity of the critical state model.

The above geometrical construction allows us to determine the temperature dependence of J_c in the temperature region just below T_c [41]. If we define that J_c(D)=1 (in arbitrary units) in the $4\pi\chi'$ curve of h_{AC}= 1 Oe, we find J_c(E) =10J_c(D) and J_c(C) =0.1J_c(D) according to the above argument. One also notices from the $4\pi\chi'$ curves shown in Fig. 13(a) that the points C, D, and E roughly represent the temperature of half screening T_{hs} under the respective ac excitation field amplitudes, i.e., T_{hs} = 37.1 K (C), 36.9 K (D) and 36.6 K(E) for h_{AC}= 0.1, 1, 10 Oe, respectively. Then the absolute values of J_c(C). J_c(D) and J_c(E) can be estimated to be 1.6, 16 and 160 A/cm^2 by assuming that for our geometry, D_c=0.5 mm, i.e, a half thickness of the sample. As shown in Fig. 14, the thus obtained J_c values show a highly concave temperature dependence, which can be tentatively fitted with $J_c \propto (1 - T/T_c)^{3/2}$ in the temperature range observed here. According to Clem *et al.* [42], J_c obeys the concave Ginzburg–Landau (GL) $(1 - T/T_c)^{3/2}$ temperature dependence in a granular superconductor in which the ratio of the Josephson-coupling energy to the superconducting condensation energy is of unity or larger. It can hence be expected that the present sample behaves as a strongly coupled homogeneous (or spatially isotropic) granular superconductor when the system is cooled below ~37 K. The inset of Fig. 14 also includes the J_c values at lower-temperature ($T \leq$ 30 K) derived from the height of the magnetization loop at zero magnetic field (see Fig. S4 in the supplementary material) on the basis of the Bean model [32] (for details see the supplementary material). The measured J_c data in the full (2–~37 K) temperature range reasonably follows the mean-field behavior predicted by the GL theory [43]:

$$J_c(T) = J_c(0)(1 - (T/T_c)^2)^{3/2}((1 + (T/T_c)^2)^{1/2}, \quad (1)$$

where $J_c(0)$ is the density of the depairing critical current at 0 K. Note that near T_c Eq. (1) reduces to the familiar GL $(1 - T/T_c)^{3/2}$ temperature dependence

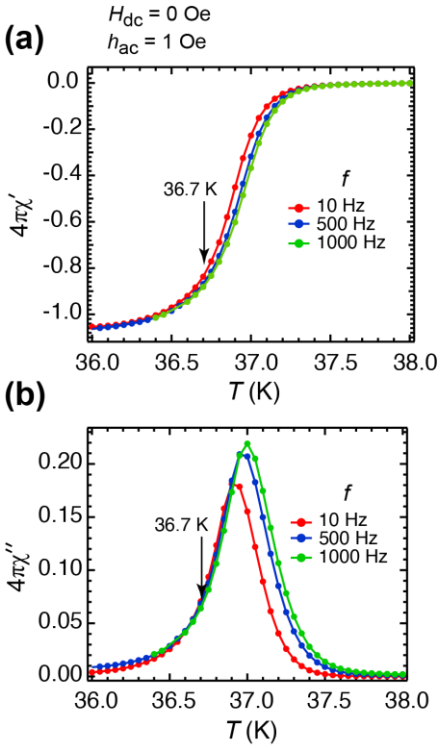

FIG. 15. Temperature dependence of the magnetic ac susceptibility [(a) $4\pi\chi'$ and (b) $4\pi\chi''$] observed in a zero dc magnetic field using an ac amplitudes h_{ac} of 1 Oe and three different ac frequencies.

[43]. The applicability of the GL theory confirms the establishment of the strongly-coupled superconductivity at temperatures below T~37 K.

In the ac susceptibility measurements, the effect of the sweep frequency f on the $4\pi\chi'$ and $4\pi\chi''$ curves is also worth investigating [44]. In general, the weak f dependence of the ac susceptibility is related to flux creep of vortices, being a slow process, contrary to the strong f dependence predicted for a linear conductor [45]. Figure 15 shows the $4\pi\chi'$ and $4\pi\chi''$ curves obtained at h_{ac}= 1 Oe under different sweep frequencies in zero static magnetic field. One sees that at temperatures above ~37 K, the $4\pi\chi'$ and $4\pi\chi''$ curves shift to higher temperatures and the transition width broadens with increasing f, also accompanied by an intensity increase in the ac loss peak. These frequency dependent features are caused by the vortex dynamic phenomena and the related dissipation processes, including conventional eddy currents, as often observed in type-II high-T_c superconductor [46,47] and a pure MgB_2 bulk sample [48]. Note, however, that when the temperature of the system goes below ~36.7 K, such a frequency dependence is not observed both in the $4\pi\chi'$ and $4\pi\chi''$ curves. This indicates that at a temperature of ~36.7 K, the system is transformed from a linear conductor into an ideal "Bean" superconductor, in which the ac susceptibility is nonlinear and frequency independent [45]. This result is in consistent with that obtained from the h_{ac} dependence given in Fig. 13. Thus, we can conclude that the critical state model is applicable to the present sample at temperatures below ~37 K, which is lower than the intragranular superconducting transition temperature (T_c=38.5 K) only by around 1.5 K.

IV. DISCUSSION

From the above observations, we have shown that the present MgO/MgB_2 nanocomposite behaves as a homogeneous bulk-like superconductor in a critical state at temperatures below ~37 K. The transition from the intra- to inter-granular regime is very smooth and is not apparently noticeable in the resistivity and susceptibility curves. These features are quite different from those of conventional granular superconductors, which generally show two-step behaviors in the temperature-dependence of resistivity and susceptibility due to the higher-temperature intragranular transition and the subsequent lower-temperature intergranular transition [49]. This two-step feature is understood in terms of a weak link model [44,50,51] or a two-level critical state model [52] assuming two distinct critical densities, i.e., a critical current density inside the grains, and another one reflecting the intergranular coupling. In general, the intergranular critical current density is much smaller than the intragranular one. As a result, magnetic flux easily penetrates along the grain boundaries or weak links [35,53], showing two-step and the related inhomogeneous superconducting properties in granular superconductors. In Ref. [22], we have also confirmed from the Hall measurements that in the normal state, the net hole density in this nanocomposite is an order smaller than that of pure MgB_2, as expected from the low volume fraction (~30%) of MgB_2. Such a low carrier density would make the sample too resistive to sustain superconductivity, as indeed observed in a MgO/MgB_2 system with ~40 wt. % of MgO [54]. Hence, the occurrence of the bulk-like superconductivity in the present MgO/MgB_2 nanocomposite implies that exceptionally strong and long-range intergranular phase locking states are established in this system, leading to a long-range-proximity-induced superconductivity.

Although it is certain that the MgO/MgB_2 fractal nanocomposite acts as a bulk-like superconductor, we still have one unanswered question. Where do the carriers in the normal phase or MgO come from? MgO is, in principle, an insulator with a large bandgap of 7.8 eV, and no carriers are present in structurally perfect

MgO. It should be noted, however, that we prepared these nanocomposites in highly Mg rich conditions using the solid-phase reaction between Mg and B_2O_3. It is hence probable that large amounts of intrinsic defects such as O vacancies and Mg interstitials are present in our sample. Such intrinsic defects in MgO can participate in both the electron and hole conductivity, causing bipolar charge transport [55]. Among other intrinsic defects, single oxygen vacancies, called F centers, and/or double oxygen vacancies, called F_2 centers, are the most likely candidates for the intrinsic defects in MgO [56–61]. Note also that McKenna and Blumberger [62] have shown from first-principles modeling that in defective MgO with a high concentration of oxygen vacancies, coherent electron tunneling is possible to occur when the separations between oxygen vacancy defects become less than 0.6 nm, accounting for the origin of long-range carrier transfer in metal oxide materials. From these considerations, we can assume that in the MgO/MgB_2 nanocomposite, there exists a large number of intrinsic defects possibly in the form of F and F_2 centers, which will contribute to the bipolar charge transport and hence to the expected Andreev reflection.

To confirm the assumption, we performed CL measurements on the polished surface of the MgO/MgB_2 nanocomposite at room temperature. It has been well documented that oxygen vacancies in MgO show a variety of luminescence properties in the ultraviolet/visible spectral regions depending on their charge states and atomic configurations [57–59, 63–65]. Hence, CL spectroscopy is a powerful technique to identify the quality and quantity of possible oxygen vacancies present in our sample.

Figures 16 and 17 show SEM images of low (3000×) and high (8000×) magnifications, respectively, along with the corresponding CL spectra. As demonstrated in Fig. 2, the gray region in the SEM images represent the MgO-regions, whereas the black regions correspond to the MgB_2-rich regions. From the position dependent CL spectra, we see that the CL emission properties vary from site to site. In the black (or MgB_2-rich) regions, we hardly observed any CL emissions [see the CL spectra of position A in Figs. 16(b) and 17(b)]. This is reasonable because MgB_2 is a metallic compound at room temperature, showing no band-gap and/or defect-related luminescence. As for the gray (or MgO-rich) regions, we typically observed two types of CL spectra. One is characterized by the CL band peaking at ~350 nm with a longer-wavelength shoulder extending to ~800 nm [see the CL spectra of position B in Figs. 16(b) and 17(b)]. The prominent CL peak at ~350 nm is assigned to the emissions from F_2 (375 nm) and/or F^+ (380 nm) centers [57–59,63], and the longer-wavelength tail to

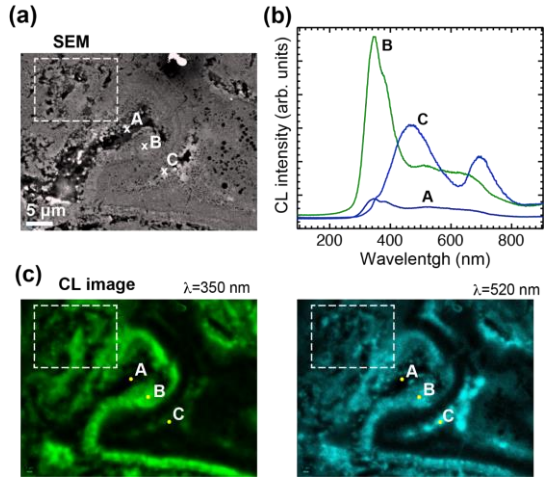

FIG. 16. (a) SEM image (3000×) and (b) the corresponding CL spectra acquired at points A, B, and C in (a). (c) CL mapping images obtained at wavelengths of 350 (left panel) and 520 (right panel) nm. White boxes in (a) and (c) indicate appropriate location used for the subsequent CL observations give in Fig. 17.

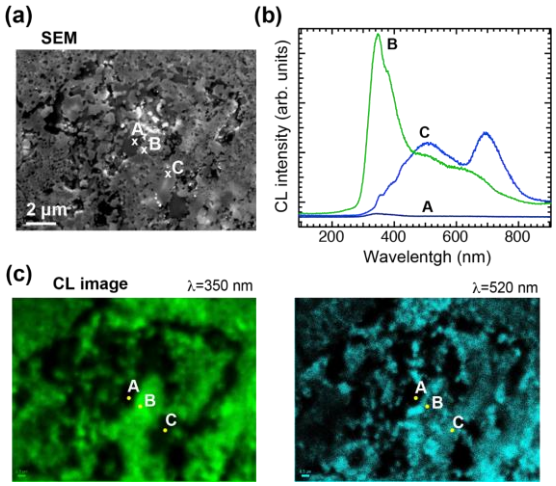

FIG. 17. (a) SEM image (8000×) and (b) the corresponding CL spectra acquired at points A, B, and C in (a). (c) CL mapping images obtained at wavelengths of 350 (left panel) and 520 (right panel) nm. These SEM and CL images are taken for the white box region given in Fig. 16.

those from F_2^{2+} (441 nm), F (490 nm) and F_2^+ (475 nm) centers [64,65]. The other type of CL spectra shows two broad CL bands at ~500 nm and ~700 nm [see the CL spectra of position C in Figs. 16(b) and 17(b)]. The CL band at ~500 nm results from the F center, with minor contributions from F_2^+, and F_2^{2+} centers, while the one at ~700 nm is probably due to the thermal detachment of holes from the Mg vacancy [66]. To

elucidate the spatial distributions of these two types of CL emissions, CL mapping images were taken at wavelengths of 350 and 520 nm, as shown in Figs. 16(c) and 17(c). Although the CL mapping images at 350 and 520 nm are not identical to each other, they are mostly overlapped, implying that F- and F_2-type centers spatially coexist. It should also be noted that these F- and F_2-type centers are not distributed homogeneously over the entire MgO-rich regions, but rather they are preferentially located around the MgB_2-rich regions, forming long and winding channels consisting of oxygen vacancies. These channel of oxygen vacancies will provide a number of carries in the MgO-rich regions, accounting for a rather low resistivity [~0.2 μΩm at T = 100 K, see Fig. 9(a)] in the normal state. Thus, we suggest that the present MgB_2/MgO interfaces behave as if they were S/N junctions, which will hence allow Andreev reflections at these interfaces.

Finally, we discuss possible structural origins for the long-range proximity effect. First, we should note that in the present nanocomposite, atomically clean MgO/MgB_2 interfaces are created, as demonstrated in a series of STEM images shown in Figs. 5–8. These atomically clean interfaces will behave as a good electric contact with lower barrier heights, which makes the Andreev reflection significant [1–3]. As seen in Fig. 8, such a clean interface can also be found at the boundary between two differently aligned MgO grains in the MgO rich region. Clean MgO/MgO interfaces will behave as elastic scatters and will provide a mechanism to re-direct the trajectories of Andreev quasiparticles to the MgO/MgB_2 interface, leading to the coherent multiple scattering effect, as proposed by van Wees and co-workers [4]. Furthermore, a complex morphology of MgB_2 primary particles, as evidenced by STEM/EDX images shown in Fig. 4(c), will also contribute to multiple Andreev scattering. The complex morphology is characterized by a negative curvature at the MgO-MgB_2 interfaces. Consequently, the expected Andreev reflections can occur multiple times between the opposite MgO/MgB_2 interfaces, which would lead to an enhanced proximity effect as in the case of 2D superconducting islands [11]. We suggest that this coherent multiple scattering will occur in a hierarchical manner in our fractal nanocomposite and is likely to be responsible for the long-range proximity effect throughout the entire sample. It has recently been elucidated that a fractal topology can provide an underlying basis for the establishment of long-range correlation and cooperation behaviors in complex systems [67–69]. The concept of fractal has often been introduced in the field of cuprate superconductors [70,71] and strongly disordered superconductors [16,72,73], where the BCS theory is difficult to apply. Our fractal nanocomposite may provide an additional experimental system, in which the quantum coherence is enhanced by fractality.

.

V. CONCLUSIONS

We have performed detailed structural and morphological characterization on the MgO/MgB_2 fractal nanocomposite. The FIB-SEM and the resulting 3D reconstructed images have elucidated that the randomly interwoven-like MgO/MgB_2 structures spread isotropically throughout the sample, showing an almost constant value of fractal dimension (D = 1.67–1.68) irrespective of the direction of the cross section inspected. Atomic-scale STEM analysis has revealed that the atomically clean MgO/MgB_2 interfaces are created in the MgO/MgB_2 nanocomposite. The interface boundaries are characterized by planar boundaries and/or terrace-and-step structures without forming interfacial amorphous regions. These clean interfaces result presumably from the motion and atomic arrangements of grain boundaries during the sintering process. We have shown from resistivity, dc and ac susceptibility, and MO measurements that at temperatures below ~37 K, the present MgO/MgB_2 nanocomposite acts as a homogeneous bulk-like superconductor in a critical state, which is preceded by an intragranular superconducting transition at 38.5 K. The strong intergrain coupling is expected to be emerged over the entire volume of the system although the sample consists of MgO and MgB_2 nanograins with complex morphologies. Also, the SEM-CL measurements have revealed the presence of large amounts of oxygen vacancies in the MgO-rich phase, forming complex long and winding channels consisting of oxygen vacancies around the MgB_2-rich phase. These channels of oxygen vacancies will allow the long-range carrier transfer via coherent tunneling and hence the long-range proximity effect due to hierarchical quantum interference of Andreev quasiparticles. The strong macroscopic phase coherence in the highly disordered MgO/MgB_2 nanocomposite could be realized due to the fortuitous combination of atomically clean interface, fractal morphology, and long channels of coherent charge transport. These structural features presumably induce long-range proximity-induced superconducting correlations, accounting for the excellent phase-coherent capability of this proximity-coupled fractal system.

SUPPLEMENTARY MATERIAL

See Supplementary Material for further details of the sample preparation, additional experimental data, the calculation procedure of local current distribution

based on an inverse Biot-Savart procedure, and the profiles of the flux density taken during the field ramp-up and ramp-down processes at different temperatures.

ACKNOWLEDGMENTS

A part of this work was conducted in Institute for Molecular Science, supported by "Advanced Research Infrastructure for Materials and Nanotechnology in Japan (ARIM)" of the Ministry of Education, Culture, Sports, Science and Technology (Proposal Numbers. JPMXP1223NM0163, JPMXP1223MS1024 and JPMXP1224MS1017). This work was also supported by NIMS Joint Research Hub Program. We also acknowledge Research Facility Center for Science and Technology, Kobe University, for providing access to the MPMS facility.

AUTHORDECLARATIONS

Conflict of Interest

The authors have no conflicts to disclose.

Author contributions

I. Nakaaki: Investigation (lead); Data curation (lead); Methodology (lead); Writing – review & editing (equal). **A. Hashimoto**: Data curation (equal); Formal analysis (equal). **S. Kondo**: Investigation (equal); Methodology (equal); Writing – review & editing (equal). **Y. Ikuhara**: Investigation (equal); Methodology (equal); Writing – review & editing (equal). **S. Ooi**: Investigation (equal); Methodology (equal); Writing – review & editing (equal). **M. Tachiki:** Investigation (equal); Methodology (equal); Writing – review & editing (equal). **S. Arisawa**: Investigation (equal); Methodology (equal); Writing – review & editing (equal). **A. Nakamura**: Investigation (equal); Methodology (equal); Writing – review & editing (equal). **T. Moronaga**: Investigation (equal); Methodology (equal); Writing – review & editing (equal). **J. Chen**: Investigation (equal); Methodology (equal); Writing – review & editing (equal). **H. Segawa**: Investigation (equal); Methodology (equal); Writing – review & editing (equal). **T. Sakurai**: Investigation (equal); Methodology (supporting). **H. Ohta**: Investigation (supporting); Methodology (equal). **T. Uchino**: Conceptualization (lead); Investigation (equal); Methodology (equal); Funding acquisition (lead); Writing – original draft (lead).

DATA AVAILABILITY

The data that support the findings of this article are available from the authors upon reasonable request.

[1] G. E. Blonder, M. Tinkham, and T. M. Klapwijk, Transition from metallic to tunneling regimes in superconducting microconstrictions: Excess current, charge imbalance, and supercurrent conversion, Phys. Rev. B **25**, 4515 (1982).

[2] H. Courtois, P. Gandit, D. Mailly, and B. Pannetier, Long-range coherence in a mesoscopic metal near a superconducting interface, Phys. Rev. Lett. **76**, 130 (1996).

[3] P. Dubos, H. Courtois, O. Buisson, and B. Pannetier, Coherent Low-Energy Charge Transport in a Diffusive S-N-S Junction, Phys. Rev. Lett. **87**, 206801 (2001).

[4] B. J. van Wees, P. de Vries, P. Magnée, and T. M. Klapwijk, Excess conductance of super-conductor-semiconductor interfaces due to phase conjugation between electrons and holes, Phys. Rev. Lett. **69**, 510 (1992).

[5] D. Montemurro, D. S. Golubev, S. Kubatkin, F. Tafuri, T. Bauch, and F. Lombardi, Enhanced Josephson coupling in hybrid nanojunctions, Phys. Rev. B **107**, 094517 (2023).

[6] L. Angers, F. Chiodi, G. Montambaux, M. Ferrier, S. Guéron, and H. Bouchiat, Proximity dc squids in the long-junction limit, J. C. Cuevas, Phys. Rev. B **77**, 165408 (2008).

[7] I. Bozovic, G. Logvenov, M. A. J. Verhoeven, P. Caputo, E. Goldobin, and M. R. Beasley, Giant Proximity Effect in Cuprate Superconductors, Phys. Rev. Lett. **93**, 157002 (2004).

[8] R. S. Decca, H. D. Drew, E. Osquiguil, B. Maiorov, and J. Guimpel, Anomalous proximity effect in underdoped $YBa_2Cu_3O_{6+x}$ Josephson junctions. Phys. Rev. Lett. **85**, 3708 (2000).

[9] B. Pannetier and H. Courtois, Andreev reflection and proximity effect, J. Low Temp. Phys. **118**, 599 (2000).

[10] T. M. Klapwijk, Proximity effect from an Andreev perspective, J. Supercond. **17**, 593 (2004).

[11] J. Kim, V. Chua, G. A. Fiete, H. Nam, A. H. MacDonald, and C.-K. Shih, Visualization of geometric influences on proximity effects in heterogeneous superconductor thin films. Nat. Phys. **8**, 464 (2012).

[12] H. Nam, C. Zhang, W. Lee, .S Zhu, H-J. Gao, Q. Niu, G. A. Fiete, and C.-K. Shih, Behavior of superconductivity in a Pb/Ag heterostructure, Phys. Rev. B **100**, 094512 (2019).

[13] J. Li, H.-B. Leng, H. Fu, K. Watanabe, T. Taniguchi, X. Liu, C.-X. Liu, and J. Zhu, Superconducting proximity effect in a transparent van der Waals superconductor-metal junction, Phys. Rev. B **101**, 195405 (2020).

[14] A. Valletta, A. Bianconi, A., Perali, G. Logvenov, G. Campi High-T_c superconducting dome in artificial heterostructures made of nanoscale quantum building blocks. Phys. Rev. B **110**, 184510 (2024).

[15] G. Campi, A. Alimenti, G. Logvenov, G. A. Smith, F. F. Balakirev, S. E. Lee, et al., Upper critical magnetic field and multiband superconductivity in artificial high-T_c superlattices of nano quantum wells Phys. Rev. Mater. **9**, 074204 (2025).

[16] G. Campi, A. Bianconi, N. Poccia, G. Bianconi, L. Barba, G. Arrighetti, D. Innocenti, J. Karpinski, N. D. Zhigadlo, S. M. Kazakov, M. Burghammer, M. v. Zimmermann, M. Sprung, A. Ricci, Inhomogeneity of charge-density-wave order and quenched disorder in a high-T_c superconductor. Nature **525**, 359 (2015).

[17] R. H. Parmenter, Size Effect in a granular superconductor, Phys. Rev. **166**, 392 (1968).

[18] I. Sternfeld, V. Shelukhin, A. Tsukernik, M. Karpovski, A. Gerber, and A. Palevski, Proximity effect in granular superconductor–normal metal structures, Phys. Rev. B **71**, 064515 (2005)

[19] S. Bose and P. Ayyub, Superconducting proximity effect in Pb/Ag nanocomposites, Phys. Rev. B **76**, 144510 (2007).

[20] Y. B. Zhang, D. F. Zhou, Z. X. Lv, Z. Y. Deng, C. B. Cai, S. P. Zhou, Electrical transport characteristics of superconducting MgB_2 – MgO composite near continuous percolation, J. Appl. Phys. **107**, 123907 (2010).

[21] T. Uchino, N. Teramachi, R. Matsuzaki, E. Tsushima, S. Fujii, Y. Seto, K. Takahashi, T. Mori, Y. Adachi, Y. Nagashima, Y. Sakaguchi, K. Ohishi, A. Koda, T. Sakurai, and H. Ohta Proximity coupling of superconducting nanograins with fractal distributions, Phys. Rev. B **101**, 035146 (2020).

[22] N. Teramachi, A. Hashimoto, I. Nakaaki, S, Ooi, M. Tachiki, S. Arisawa, Y. Seto, T. Sakurai, H. Ohta, J. Valenta, N. Tsujii, T. Mori, and T. Uchino, Strong phase coherence and vortex matter in a fractal system with proximity-induced superconductivity, Phys. Rev. B **108**, 155146 (2023).

[23] O. Guillon, J. Gonzalez-Julian, B. Dargatz, T.Kessel, G. Schierning, J. Räthel, M. Herrmann, Field-assisted sintering technology/spark plasma sintering: mechanisms, materials, and technology developments, Ad. Eng. Mater. **16**, 830 (2014).

[24] L. Priester, *Grain Boundaries: From Theory to Engineering* (Springer, Dordrecht, 2013).

[25] Y. Ikuhara, Grain boundary and interface structures in ceramics, J. Ceram. Soc. Jpn. **109**, S110-S120 (2001).

[26] M. L. Bowers, C. Ophus, A. Gautam, F. Lançon, and U. Dahmen, Step Coalescence by Collective Motion at an Incommensurate Grain Boundary, Phys. Rev. Lett. **116**, 106102 (2016).

[27] T. J. Rupert, D. S. Gianola, Y. Gan, and K. J. Hemker, Experimental observations of stress-driven grain boundary migration, Science **326**, 1686 (2009).

[28] H. Sternlicht, W. Rheinheimer, M.J. Hoffmann, and W. D. Kaplan, The mechanism of grain boundary motion in $SrTiO_3$, J. Mater. Sci. **51**, 467 (2016).

[29] Q. Huang, Q. Zhu, Y. Chen, M. Gong, J. Li, Z. Zhang, W.Yang, J. Wang, H. Zhou, and J/ Wang, Twinning-assisted dynamic adjustment of grain boundary mobility, Nat. Commun. **12**, 6695 (2021).

[30] Z. Fang, J. Xiao, S. Tan, C. Deng, G.Wang, S. X Mao, Atomic-scale observation of dynamic grain boundary structural transformation during shear-mediated migration, Sci. Adv. **8**, eabn3785 (2022).

[31] F. M. Araujo-Moreira, C. Navau, and A. Sanchez, Meissner state in finite superconducting cylinders with uniform applied magnetic field, Phys. Rev. B **61**, 634 (2000).

[32] C. P. Bean, Magnetization of high-field superconductors, Rev. Mod. Phys. **36**, 31 (1964).

[33] P. W. Anderson and Y. B. Kim, Hard Superconductivity: Theory of the Motion of Abrikosov Flux Lines, Rev. Mod. Phys. **36**, 39 (1964).

[34] L. Ji, R. H. Sohn, G. C. Spalding, C. J. Lobb, and M. Tinkham, Critical-state model for harmonic generation in high-temperature superconductors, Phys. Rev. B **40**, 10936 (1989).

[35] Ch. Jooss, J. Albrecht, H. Kuhn, S. Leonhardt, and H. Kronmüller, Magneto-optical studies of current distributions in high-Tc superconductors, Rep. Prog. Phys. **65**, 651 (2002).

[36] J. W. Zuber, F. S. Wells, S. A. Fedoseev, T. H. Johansen, A. B. Rosenfeld, and A. V. Pan, A new approach to the inverse problem for current mapping in thin-film superconductors, J. Appl. Phys. **123**, 123906 (2018).

[37] Th. Schuster, M. R. Koblischka, N. Moser, H. Kronmüller, Observation of nucleation and annihilation of flux-lines with opposite sign in high-T_c superconductors, Physica C **179**, 269 (1991).

[38] M. E. Gaevski, A. V. Bobyl, D. V. Shantsev, Y. M. Galperin, T. H. Johansen, M. Baziljevich, H. Bratsberg, and S. F. Karmanenko,, Magneto-optical study of magnetic-flux penetration into a current-carrying high-temperature-supercon-

ductor strip, Phys. Rev. B **59**, 9655 (1999).
[39] K.-H. Müller , AC susceptibility of high temperature superconductors in a critical state model, Physica C **159**, 717 (1989).
[40] A. Schindler, R. König, T. Herrmannsdörfer, and H. F. Braun, Inter- and intragranular effects in superconducting compacted platinum powders, Phys. Rev. B **62**, 14350 (2000).
[41] L. Civale, T. K. Worthington, L. Krusin-Elbaum, and F. Holtzberg, in Magnetic Susceptibility and Other Spin Systems, edited by R. A. Hein, T. L. Francavilla, and D. H. Liebenberg (Plenum, New York, 1991), p. 313.
[42] J. R. Clem, B. Bumble, S. I. Raider, W. J. Gallagher, and Y. C. Shih, Ambegaokar-Baratoff–Ginzburg-Landau crossover effects on the critical current density of granular superconductors, Phys. Rev. B **35**, 6637 (1987).
[43] W. J. Skocpol; M. R. Beasley; M. Tinkham. Self-heating hotspots in superconducting thin-film microbridges,, J. Appl. Phys. **45**, 4054 (1974).
[44] K.-H. Müller Frequency dependence of AC susceptibility in high-temperature superconductors: Flux creep and critical state at grain boundaries, Physica C **168**, 585 (1990).
[45] E. H. Brandt, Susceptibility of superconductor disks and rings with and without flux creep, Phys. Rev. B **55**, 14513 (1997).
[46] E. H Brandt, The flux-line lattice in superconductors, Rep. Prog. Phys. **58**, 1465 (1995).
[47] R. B. Goldfarb, M. Lelental, and C. A. Thompson, in *Magnetic Susceptibility of Superconductors and Other Spin Systems*, edited by R. A. Hein et al., (Plenum, New York, 1991), p. 49.
[48] M. J. Qin, X. L. Wang, S. Soltanian, A. H. Li, H. K. Liu, and S. X. Dou, Dependence of the flux-creep activation energy on current density and magnetic field for the MgB_2 superconductor, Phys. Rev. B **64**, 060505(R), (2001).
[49] W. Y. Shih, C. Ebner, and D. Stroud, Frustration and disorder in granular superconductors, Phys. Rev. B **30**, 134 (1984).
[50] K. K. Likharev, Superconducting weak links, Rev. Mod. Phys. **51**, 101 (1979).
[51] E. A. Early, C. C. Almasan, R. F. Jardim, and M. B. Maple, Double resistive superconducting transition in $Sm_{2-x}Ce_xCuO_{4-y}$, Phys. Rev. B **47**, 433(1993).
[52] L. Ji, M. S. Rzchowski, N. Anand, and M. Tinkham, Magnetic-field-dependent surface resistance and two-level critical-state model for granular superconductors, Phys. Rev. B **47**, 470 (1993).
[53] D. C. Larbalestier, L. D. Cooley, M. O. Rikel, A. A. Polyanskii, J. Jiang, S. Patnaik, X. Y. Cai, D. M. Feldmann, A. Gurevich, A. A. Squitieri, M. T. Naus, C. B. Eom, E. E. Hellstrom, R. J. Cava, K. A. Regan, N. Rogado, M. A. Hayward, T. He, J. S. Slusky, P. Khalifah, K. Inumaru, and M. Haas, Strongly linked current flow in polycrystalline forms of the superconductor MgB_2, Nature **410**, 186 (2001).
[54] D. K. Singh, B. Tiwari, R. Jha, H. Kishan, and V. P. S. Awana, Role of MgO impurity on the superconducting properties of MgB_2, Physica C 505, 104 (2014).
[55] T. V. Perevalov, D. R. Islamov, T. M. Zalyalov, A. A. Gismatulin, V. A. Golyashov, O. E. Tereshchenko, D. V. Gorshkov, and V. A. Gritsenko , Electron and hole bipolar injection in magnesium oxide films, Appl. Phys. Lett. 124, 042903 (2024).
[56] F. Schleicher, U. Halisdemir, D. Lacour, M. Gallart, S. Boukari, G. Schmerber, V. Davesne, P. Panissod, D. Halley, H. Majjad, Y. Henry, B. Leconte, A. Boulard, D. Spor, N. Beyer, C. Kieber, E. Sternitzky, O. Cregut, M. Ziegler, F. Montaigne, E. Beaurepaire, P. Gilliot, M. Hehn, and M. Bowen , Localized states in advanced dielectrics from the vantage of spin- and symmetry-polarized tunnelling across MgO, Nat. Commun. **5**, 4547 (2014).
[57] T. Uchino, D. Okutsu, Broadband Laser Emission from Color Centers Inside MgO Microcrystals, Phys. Rev. Lett. **101**, 117401 (2008).
[58] Y. Uenaka,T. Uchino, Photoexcitation, trapping, and recombination processes of the *F*-type centers in lasing MgO microcrystals, Phys. Rev. B **83**, 195108 (2011).
[59] H. Soma, Y. Uenaka, A. Asahara, T. Suemoto, and T. Uchino, Ultraviolet stimulated emission from high-temperature-annealed MgO microcrystals at room temperature, Appl. Phys. Lett. **106**, 041116 (2015).
[60] K. P. McKenna and A. L. Shluger,, Electron-trapping polycrystalline materials with negative electron affinity, Nat. Mater. **7**, 859 (2008).
[61] K. P. McKenna and A. L. Shluger, First-principles calculations of defects near a grain boundary in MgO, Phys. Rev. B **79**, 224116 (2009).
[62] K. P. McKenna1, and J. Blumberger, Crossover from incoherent to coherent electron tunneling between defects in MgO, Phys. Rev. B **86**, 245110 (2012).
[63] R. González, M. A. Monge, J. E. Muñoz Santiuste, R. Pareja, Y. Chen, E. Kotomin, M. M. Kukla, and A. I. Popov, Photoconversion of F-

type centers in thermochemically reduced MgO single crystals, Phys. Rev. B **59**,4786 (1999).
[64] D. O. O'Connell, B. Henderson, J. M. Bolton, Uniaxial stress and polarisation studies of F_2 centre luminescence in MgO, Solid State Commun. **38**, 283 (1981).
[65] J. D. Bolton, B. Henderson, D. O. O'Connell, Photoluminescence of F_2^{2+} centres in additively coloured magnesium oxide, Solid State Commun. **38**, 287 (1981).
[66] A. A. Tatarintsev, E. Yu. Zykova, A. E. Ieshkin, V. A. Kiselevskiy, N. G. Orlikovskaya, Electrizaton and cathodoluminescence of single crystal MgO under 2.5 – 15 keV electron beam, Appl. Surf. Sci. **660**, 159964 (2024).
[67] F. C. Santos and J. M. Pacheco, Scale-free networks provide a unifying framework for the emergence of cooperation, Phys. Rev. Lett. **95**, 098104 (2005).
[68] C. Song, S. Havlin, and H. A. Makse, Origins of fractality in the growth of complex networks, Nat. Phys. **2**, 75 (2006).
[69] Y. Khaluf, E. Ferrante, P. Simoens and C. Huepe, Scale invariance in natural and artificial collective systems: a review, Interface **14**, 20170662 (2017).
[70] M. Fratini, N. Poccia, A. Ricci, G. Campi, M. Burghammer, G. Aeppli, and A. Bianconi, Scale-free structural organization of oxygen interstitials in La_2CuO_{4+y}, Nature **466**, 841 (2010)..
[71] N. Poccia, M. Fratini, A. Ricci, G. Campi, L. Barba, A. Vittorini-Orgeas, G. Bianconi, G. Aeppli, and A, Bianconi, Evolution and control of oxygen order in a cuprate superconductor, Nat. Mater. **10**, 733 (2011).
[72] M. V. Feigel'man, L. B. Ioffe, V. E. Kravtsov, and E. Cuevas, Fractal superconductivity near localization threshold, Ann. Phys. **325**, 1390 (2010).
[73] V. D. Neverov, A. E. Lukyanov, A. V. Krasavin, A. Vagov, and M. D. Croitoru, Spatial correlations in disorder: Impact on the superconducting critical temperature, Phys. Rev. B **111**, 184514 (2025).